Nanoscale

PAPER

Cite this: *Nanoscale*, 2019, **11**, 6101

Intrinsic ferromagnetism and topological properties in two-dimensional rhenium halides

Qilong Sun* and Nicholas Kioussis *

Received 10th January 2019,
Accepted 1st March 2019

DOI: 10.1039/c9nr00315k

rsc.li/nanoscale

The realization of robust intrinsic ferromagnetism in two-dimensional (2D) materials in conjunction with the intriguing quantum anomalous Hall (QAH) effect has provided a fertile ground for novel physics and for the next-generation spintronic and topological devices. On the basis of density functional theory (DFT), we predict that layered 5d transition-metal heavier halides (TMHs), such as ReX_3 (X = Br, I), show intrinsic ferromagnetism with high spin polarization and high Curie temperatures. The outstanding dynamic and thermodynamic stability ensures their experimental feasibility. The strong spin–orbit coupling (SOC) of Re makes the electronic structure of the ReI_3 monolayer topologically nontrivial with a large Chern number ($C = -4$). DFT+U calculations reveal that the 2D system undergoes a nontrivial to trivial transition with increasing on-site Hubbard Coulomb interaction U through the emergence of a Dirac cone. This transition is corroborated by the emergence of chiral edge states and the anomalous Hall conductivity. These findings not only demonstrate room-temperature ferromagnetism in atomically thin 5d TMHs, but also pave the way for the potential realization of the QAH effect with high Chern numbers in pristine 2D layers.

Introduction

Two-dimensional (2D) materials have been the subject of intensive studies in the past decade because of their novel physics and unique properties compared to their bulk counterparts.[1–4] With numerous types of condensed-matter behavior that have been observed in pristine 2D crystals, intrinsic polarization or ferromagnetic ordering has been notably absent as the Mermin–Wagner theorem excludes the long-range magnetic order by thermal fluctuations.[5] This limitation greatly hinders the utilization of these novel 2D nanosheets in the field of spintronic nanodevices. To this end, 2D ferromagnetic materials with desirable magnetic and electronic properties are highly needed.

Recently, 2D magnets down to the few-monolayer limit have been successfully demonstrated by exfoliating bulk magnetic van der Waals (vdW) crystals such as $Cr_2Ge_2Te_6$ and CrI_3.[6,7] However, these 2D materials are ferromagnetic insulators with rather low Curie temperatures,[8] T_C, of 45 K and 90 K, respectively. Besides, if exposed to air CrI_3 flakes degrade rapidly, thus severely hampering the fabrication and exploration of CrI_3-based devices. Actually, most technological applications require room temperature magnetic ordering and good physical stability. Consequently, intense experimental and theoretical efforts have recently focused on searching for ferromagnetic 2D materials, which combine high spin polarization, robust long-range ordering and high T_C.

Furthermore, 2D magnets provide a platform to study novel phenomena in magnetism, including the quantum anomalous Hall (QAH) effect associated with robust chiral edge states. The synergy between the onset of intrinsic ferromagnetism which breaks the time-reversal symmetry and the strong spin–orbit coupling (SOC) in 2D materials can trigger an insulating state with a topologically nontrivial band structure characterized by a nonzero Chern number.[9] The dissipationless charge transport in QAH insulators without the need for an external magnetic field provides promising applications in low-energy consumption spintronics. Currently, the realization of the QAH effect in solid-state materials can only be achieved at extremely low temperatures (below 100 mK) because of the small topologically nontrivial band gap.[10,11] Therefore, to enable potential device applications, it is important to identify materials for the QAH effect with a larger band gap and a high Curie temperature (T_C).

The family of layered transition-metal halides (TMHs) paved the way for a wide range of magnetic ordering in 2D systems.[12,13] However, current studies have mainly focused on 3d-transition metal-based 2D TMHs.[14–18] On the other hand, the emergence of magnetism and non-trivial topological properties in 5d transition-metal TMHs which have larger SOC remains an open question.

The objective of this work is to investigate the structural, electronic, magnetic, and topological properties of 2D rhenium

Department of Physics and Astronomy, California State University, Northridge, CA 91330, USA. E-mail: long.q.sun@gmail.com, nick.kioussis@csun.edu

trihalides by means of density functional theory (DFT), *ab initio* molecular dynamics, and Monte Carlo simulations, respectively. We find that heavier halides (Br, I) are dynamically and thermodynamically stable in contrast to the unstable phonon modes for lighter halides (F, Cl). Furthermore, we demonstrate that ReX_3 (X = Br, I) are half-metals with a large bandgap in one spin channel based on the PBE functional and exhibit both high Curie temperatures and a high Chern number ($C = -4$). DFT+U calculations reveal that the Chern number decreases with increasing on-site Hubbard Coulomb interaction U, vanishing at a critical U_{eff} value where the 2D system undergoes a nontrivial to trivial transition through the emergence of a Dirac cone. Further analysis of the nontrivial gapless chiral edge states and the QAH conductivity provides compelling evidence for the experimental realization of the QAH effect in heavier rhenium trihalides and their potential for future applications in electronic and spintronic devices.

Computational method

Spin-polarized first-principles electronic structure calculations were performed using the plane-wave basis code Vienna *ab initio* simulation package (VASP) with the projector augmented-wave (PAW) scheme.[19,20] The generalized gradient approximation (GGA), as formulated by Perdew–Burke–Ernzerhof (PBE), was used to treat the exchange and correlation functional.[21] We applied periodic boundary conditions and a vacuum region of 20 Å thickness along the z direction to simulate the 2D structures. The kinetic energy cutoff was set at 500 eV, and the Brillouin zone (BZ) integration was sampled with a 23 × 23 × 1 Γ-centered Monkhorst–Pack grid.[22] All structures were fully relaxed until the residual forces on each atom are less than 0.01 eV $Å^{-1}$ and the total energy is converged to less than 10^{-6} eV per formula unit.

GGA+U calculations were used to account for the exchange and correlation for the Re-5d orbital, where only a single effective $U_{eff} = U - J$ parameter accounts for the Coulomb interaction, neglecting thereby any higher multi-polar terms.[23] The Berry curvatures and edge states were calculated employing an effective tight-binding Hamiltonian with spin orbit coupling derived from maximally localized Wannier functions (MLWF) *via* the WANNIER90 and Wannier-Tools packages, respectively.[24,25] The phonon dispersions were calculated using the finite displacement approach implemented in the PHONOPY code.[26] In order to investigate the thermal stability *ab initio* molecular dynamics (AIMD) simulations using supercells were also carried out for 10 ps (with a time step of 2 fs) at 600 K.

Results and discussion

The 2D crystal structure of the ReX_3 (X = Br and I) monolayer (denoted as ML), shown in Fig. 1(a), was assumed to be similar to the hexagonal lattice of CrI_3,[7] where each Re atom is bonded with six X atoms leading to a distorted octahedron. The Re atomic layer is sandwiched between two X atomic layers with two Re and six X atoms per (1 × 1) unit cell. Table 1

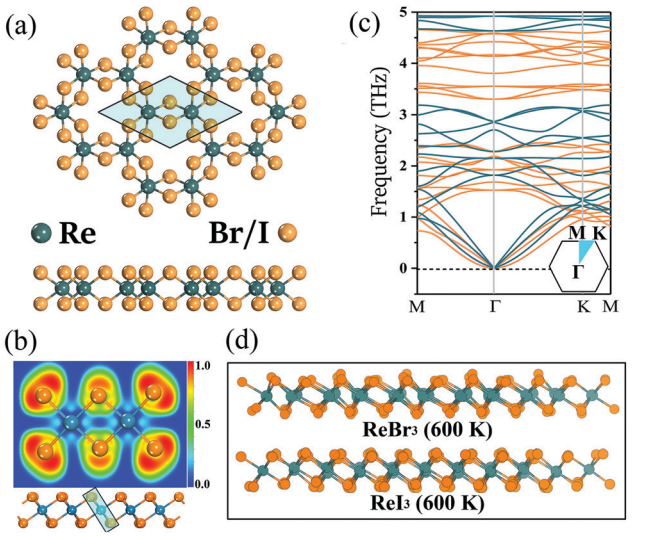

Fig. 1 (a) Top and side views of the crystalline structure of the ReX_3 (X = Br, I) ML. The solid lines denote the unit cell. (b) Electron localization function (ELF) of ReI_3, where ELF = 1 (red) and 0 (blue) indicate accumulation and depletion of the electron density, respectively. (c) Phonon spectrum of $ReBr_3$ (blue curves) and ReI_3 (orange curves) MLs. (d) Side view of atomic structure snapshots from the AIMD simulations after 10 ps at 600 K for the $ReBr_3$ and ReI_3 ML.

Table 1 Calculated equilibrium lattice constant, a, Re–X bond lengths, d_{ReX}, angles of the Re–X–Re bond, cohesive energy, E_{coh}, for the FM ground state. We also list the values of the energy difference between the FM and AFM-ZZ state, $\Delta E = E_{AFM-ZZ} - E_{FM}$

	a (Å)	d_{ReX} (Å)	∠X–Re–X (°)	E_{coh} (meV per atom)	ΔE (meV)
$ReBr_3$	6.414	2.555	92.85	−3.09	90.68
ReI_3	6.957	2.738	94.33	−2.76	38.96

lists the values of the equilibrium lattice constants, the Re–X bond lengths, and the X–Re–X angle for the ferromagnetic (FM) phase, which is found to be the ground state (see below). The equilibrium lattice constants of 6.414 and 6.957 Å for $ReBr_3$ and ReI_3, respectively, are smaller than those for $CrBr_3$ (6.433 Å) and CrI_3 (7.008 Å) monolayers.[18] Consequently, this leads to shorter Re–X bond lengths suggesting stronger chemical bonding in the ReX_3 family, which will in turn help stabilize the honeycomb structures. This is corroborated by the electron localization function (ELF) of the ReI_3 ML, for example, shown in Fig. 1(b), demonstrating the charge density localization in the vicinity of the I anion and the absence of the charge density between the Re and I atoms. This in turn reflects the ionic bonding character, where each Re atom donates three electrons to its six I bonded atoms.

In order to assess the stability of the 2D ReX_3 monolayer, first we have calculated the cohesive energy, $E_{coh} = \left(E_0 - \sum_i N_i\mu_i\right)/N$, where E_0 is the total equilibrium energy, N_i and μ_i are the number and the chemical potential of

the ith type of atoms, respectively, and $N = \sum_i N_i$ is the total number of atoms in the unit cell.[27] The cohesive energy values of −3.09 and −2.76 eV per atom, listed in Table 1, for $ReBr_3$ and ReI_3, respectively, are comparable to those of silicene,[28] phosphorene,[29] and manganese trihalides,[30] indicating that the ReX_3 monolayers will form a strongly bonded network. In order to corroborate the dynamic and thermodynamic stability of the FM ground state of the ReX_3 ML, we have carried out both phonon calculations and *ab initio* molecular dynamics (AIMD) simulations, respectively. The phonon dispersions of $ReBr_3$ and ReI_3, shown in Fig. 1(c), show no imaginary frequency conforming to the dynamic stability. On the other hand, we find an imaginary frequency at the Γ point for both the lighter members (X = F, Cl), implying that they are not stable structures. Fig. 1(d) shows the AIMD snapshots of the atomic configurations of the $ReBr_3$ and ReI_3 ML, showing that the ML can maintain its structural integrity throughout a 10 ps AIMD simulation up to 600 K. Therefore, this family of materials would possess excellent thermodynamic stability. It is important to emphasize that significant progress has recently been made in the crystal growth of analogous layered materials, which share similar hexagonal structures, using the chemical vapor transport (CVT) technique, such as single crystals of $CrCl_3$ and CrI_3 and single-layer rhenium dichalcogenides (ReS_2 and $ReSe_2$).[31–34] Furthermore, the primitive units of the ReI_3 layers, namely the [ReI_6] octahedral structure, have already been synthesized in the laboratory.[35] Consequently, ReX_3 may provide a promising platform for an experimental realization at room temperature.

The values of the Re–X–Re angle for $ReBr_3$ and ReI_3, listed in Table 1, are 92.85 and 94.33, respectively. According to the Goodenough–Kanamori–Anderson (GKA) rules, the superexchange interaction of a 90° cation–anion–cation angle favors FM ordering, whereas a 180° angle favors antiferromagnetic ordering.[36–38] Thus, the superexchange interactions between two nearest-neighbor (NN) Re atoms mediated by X are expected to be dominant leading to the FM ground state. To determine the magnetic ground state, we have carried out total-energy spin-polarized calculations using a rectangular supercell (Re_4I_{12}) for the FM phase and three antiferromagnetic (AFM) phases including the AFM-Néel (AFM-N), the AFM-zigzag (AFM-ZZ), and the AFM-stripy (AFM-SR) phases, shown in Fig. 2(a). The calculations reveal that for both $ReBr_3$ and ReI_3, the FM is the ground state with a total magnetic moment of $8\mu_B$ per unit cell ($\sim 2\mu_B$ per Re atom). The next highest-energy phase is the AFM-ZZ, where the values of $\Delta E = E_{\text{AFM-ZZ}} - E_{\text{FM}}$ are listed in Table 1.

To study the temperature-dependent magnetic ordering and the Curie temperature, we employed Monte Carlo (MC) simulations of the 100 × 100 2D Ising Hamiltonian, $H = -\sum_{i,j} J_{i,j} S_i S_j$, where $J_{i,j}$ is the nearest-neighbor exchange coupling constant, and S_i and S_j are the spins at sites i and j, respectively. The *ab initio* calculated nearest-neighbor exchange interactions are 11.3 and 4.87 meV for $ReBr_3$ and

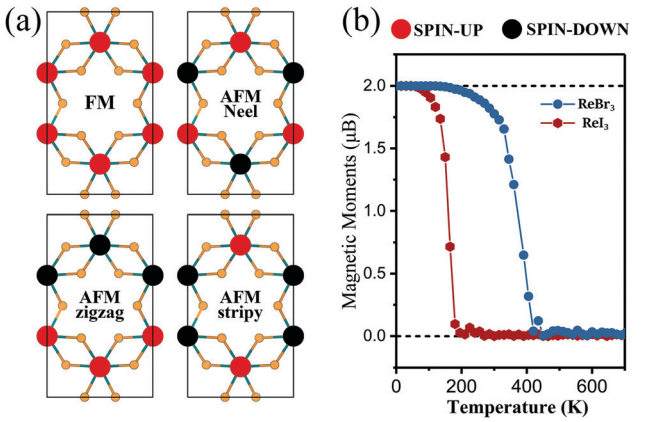

Fig. 2 (a) Top view of the FM phase and various AFM spin configurations, AFM-Néel, AFM-stripy, and AFM-zigzag, of the 2D ReX_3 ML. Here, the red (black) circles denote the up (down) spins. (b) Variation of the Re magnetic moment with temperature.

ReI_3, respectively. The temperature variation of the Re magnetic moment for the $ReBr_3$ and ReI_3 ML is shown in Fig. 2(b). We find that the Curie temperature is 390 K (165 K) for $ReBr_3$ (ReI_3), which is comparable to that of other 2D FM MLs.[18,30,39–41] On the other hand, this trend of T_c is in contrast to the increase of T_c on going down the halogen column in the 2D CrX_3 and MnX_3 ML.[16,29,42]

To gain deeper insight into the nature of FM ordering, we show in Fig. 3(a) and (b) the spin-resolved band structure and the density of states of $ReBr_3$ and ReI_3, respectively, employing the PBE exchange-correlation functional. We find that in both materials, the majority-spin channel is insulating with a rather large gap of about 1.9 eV, while the minority-spin channel is metallic, indicating that ReX_3 are half-metals with full spin polarization. The spin density distribution for the $ReBr_3$ ML shown in the inset of Fig. 3(a) is localized primarily around the Re atom and is small near the I atom. The spin-resolved density of states (DOS) of the $ReBr_3$ and ReI_3 ML reveals that the spin-minority states are mainly dominated by the 5d orbitals of Re atoms. The crystal field of the triangular antiprismatic ligand environment splits the 5d orbitals of Re into a triplet low-lying (d_{xy}, $d_{x^2-y^2}$, and d_{z^2}) orbital and a doublet high-lying (d_{yz} and d_{xz}) orbital. The orbital-resolved band structure of ReI_3 ML, shown in Fig. 3(c), shows that the bands near the Fermi level arise primarily from the hybridization of Re-derived occupied d_{z^2} and unoccupied d_{xz}. Each Re atom retains four valence electrons after forming an ionic bonding with the Re or I, where three valence electrons occupy the spin-majority triplet d_{xy}, $d_{x^2-y^2}$, and d_{z^2} derived bands and the fourth occupies the spin-minority d_{z^2} derived band. This in turn results in a low-spin state with $2\mu_B$ per Re atom, which is different from the high-spin Mn^{3+} configuration in MnX_3 ML.[30]

Next, we turn our attention to the influence of spin–orbit coupling (SOC) on the electronic structure. Theoretical studies have suggested that the SOC induces a gap opening in the spin-gapless states, leading in turn to the QAH effect.[11,43] In

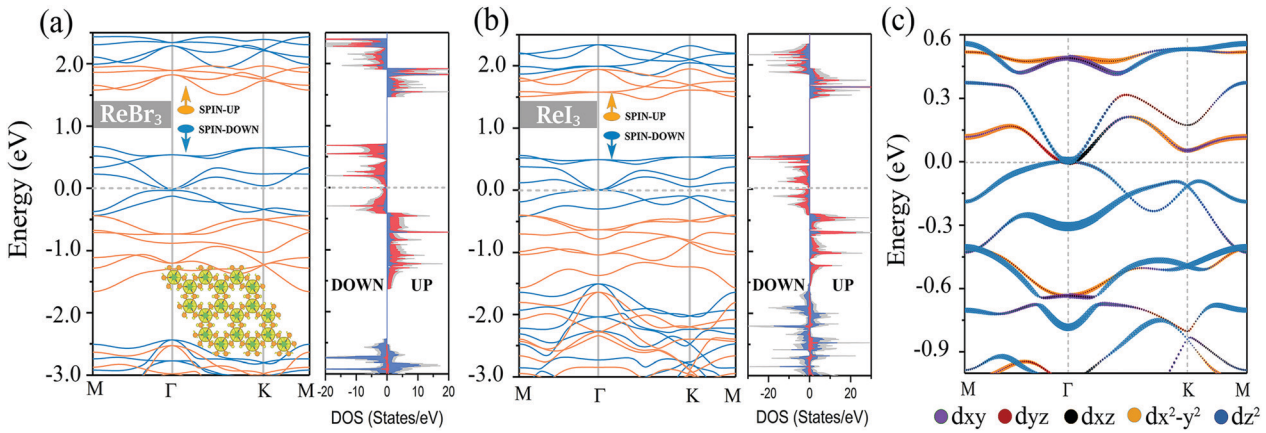

Fig. 3 (a) and (b) Spin-resolved band structure and the corresponding atom-resolved DOS [red (blue) denote Re- (X-) derived states] of the 2D $ReBr_3$ and ReI_3 FM state. The inset shows the spin density (isovalue of 0.04 e Å^{-3}) of the $ReBr_3$ ML. (c) Energy- and k-resolved distribution of the Re 5d-derived orbitals along the high-symmetry lines. The color intensity represents the amplitude of the d-orbital character. The Fermi level is denoted by a dashed line.

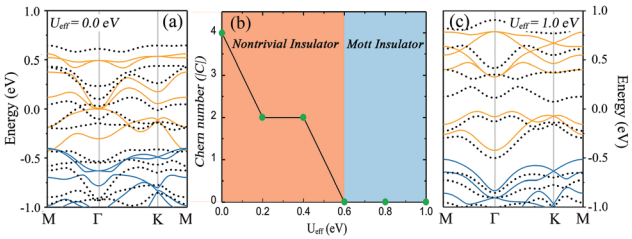

Fig. 4 (a) Band structure of the ReI_3 ML with U_{eff} = 0 eV, where the blue and orange curves denote the majority- and minority-spin bands, respectively, without SOC. The band structure in the presence of SOC is indicated with dashed curves. (b) Calculated Chern invariant (|C|) of the ReI_3 ML as a function of U_{eff} with SOC. (c) Band structure of ReI_3 ML with U_{eff} = 1.0 eV, where the bands denoted with blue (orange) are the majority-(minority-) spin bands in the absence of SOC, while the dashed ones are the bands with SOC.

Fig. 4(a), we show the band structure of the ReI_3 ML as an example with and without SOC. The large SOC of both Re and I atoms changes the band dispersion dramatically. The SOC induces a gap of 72 meV at the Γ point and shifts the valence band maximum (VBM) and the conduction band minimum (CBM) to about $\frac{1}{3}\overline{\Gamma M}$ with a gap of 10 meV.

To identify the topological properties of the gapped state, we have calculated the Chern invariant of ReI_3 using maximally localized Wannier functions.[24] The Chern invariant is obtained by integrating the Berry curvature $\Omega_z(k)$ over the Brillouin zone (BZ),[44]

$$C = \frac{1}{2\pi}\int_{BZ} d^2k\Omega_z(k) \quad (1)$$

Our calculations reveal that $C = -4$ for ReI_3, indicating that it is a QAH insulator with a topological nontrivial gap. The high Chern number identified in the ReI_3 ML may give rise to different topological phases and new fundamental physics, such as enhanced anomalous Hall conductivity (AHC) due to the associated four edge states threading through the bulk gap. In order to treat the strong on-site Coulomb interaction of the localized 5d electrons, we have also carried out GGA+U electronic structure calculations, where the effective Hubbard U_{eff} was varied from 0.0 to 1.0 eV. In the absence of SOC, the correlation energy U_{eff} triggers a gap opening in the minority-spin channel at Γ, which increases with increasing U_{eff}. We have also employed the more computationally intensive Heyd–Scuseria–Ernzerhof hybrid functional (HSE06)[45] to calculate the band structures. The results show that the energy bands for the HSE06 functional have similar dispersion to those for the PBE+U, and the only difference is the calculated band gap of the minority spin channel, indicating that the PBE+U functional is reliable. Considering that the HSE06 functional may overestimate the band gap, we have therefore used the computationally more affordable PBE+U method to investigate the electronic and topological properties of 2D rhenium halides.[46] Fig. 4(c) shows the band structure of the ReI_3 ML with and without SOC for U_{eff} = 1 eV. In the absence of SOC, the four unoccupied minority-spin bands shift away from the Fermi level, resulting in a gap opening up to 0.41 eV. In the presence of SOC, these four bands split into separate bands in the energy range from 0.072 to 0.91 eV. The variation of the Chern number for the ReI_3 ML as a function of U_{eff} is shown in Fig. 4(b). We find that the nontrivial states with a large Chern number emerge at the Fermi level when U_{eff} < 0.6 eV. Upon further increasing the effective on-site Hubbard Coulomb interaction, the Chern number decreases and vanishes at the critical U_{eff}^{crit} = 0.6 eV, where the 2D system undergoes a transition from the nontrivial to the trivial topological phase. In the nontrivial states, the fundamental bandgap initially increases with U_{eff}, then decreases below the U_{eff}^{crit} and vanishes at U_{eff}^{crit} = 0.6 eV, where the system undergoes a transition to the Mott insulating state. The fundamental gap at Γ further increases for U_{eff} > U_{eff}^{crit}. A similar continuous topological

quantum phase transition was reported in $OsCl_3$ but with a smaller U_{eff} critical value.[47]

The non-zero Chern number for U_{eff} < 0.6 eV is linked to the number of nontrivial chiral edge states that emerge inside the bulk gap of the semi-infinite system.[11] In order to gain insight into the effect of U_{eff} on the nature of the topological state, we have investigated the emergence of edge states in the 2D ribbon using an iterative procedure to calculate the Greens function for a semi-infinite system. Fig. 5(a) shows the band structures of the zigzag (left panel) and armchair (right panel) edges of the 2D ReI_3 ribbon with U_{eff} = 0.4 eV. It is clear that two gapless chiral edge states emerge in the vicinity of the Fermi level connecting the valence and conduction bands of the 2D system, which is consistent with the value of 2 for the Chern number in Fig. 4(b), indicating that ReI_3 is in the QAH phase.[48] The band structure of the ReI_3 ML for U_{eff}^{crit} = 0.6 eV (where C = 0) is shown in Fig. 5(b). One can see that the conduction and valence bands merge at the Fermi level, leading to the formation of a Dirac point at the Γ point. The emergence of a Dirac cone at U_{eff}^{crit} = 0.6 eV only in the minority-spin channel makes the 2D system half-metallic with 100% spin polarization and high-mobility carriers. Besides, U_{eff}^{crit} can be modified *via* the application of engineering strain in the interfaces of ReX_3 with other materials, resulting in the change of 2D topological properties. The Chern number C is an integer and gives rise to the quantization of the AHC, $\sigma_{xy} = Ce^2/h$. Even though the ReI_3 ML is in the trivial state for U_{eff} > 0.6 eV, Fig. 5(c) shows the AHC as a function of the position of the Fermi level, $\Delta\mu = \mu - E_F$ (E_F is the Fermi level), for U_{eff} = 0.8 eV. Interestingly, we find that when it is raised in the range from 0.2 to 0.3 eV it leads to a gap opening of 73 meV (consistent with the band structure in Fig. 4(c)) and to an AHC plateau value of −2, indicating that electron doping can induce a trivial to topological transition above room temperature.

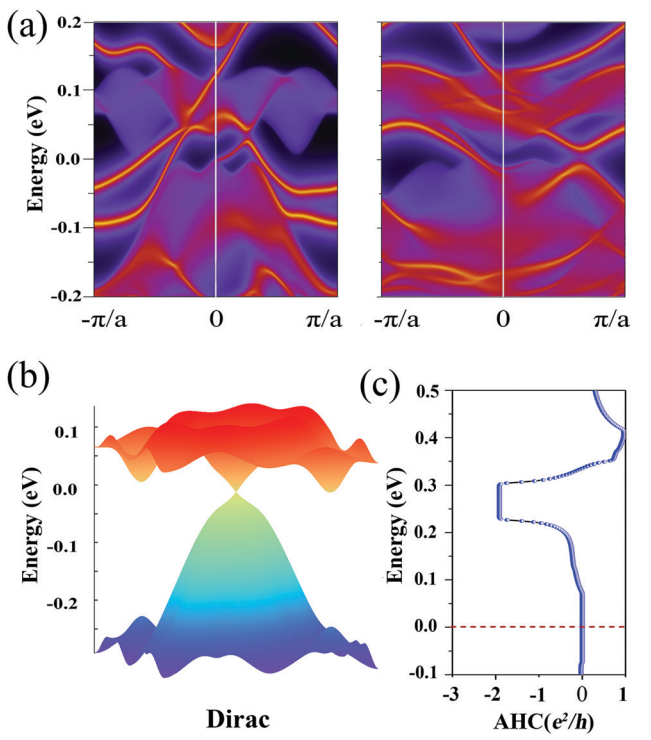

Fig. 5 (a) Band structure of the zigzag (left panel) and armchair (right panel) edge states of the 2D ReI_3 ribbon with U_{eff} = 0.4 eV. The Fermi level is set at zero. (b) 3D band structure of the ReI_3 ML with SOC and U_{eff} = U_{eff}^{crit} = 0.6 eV showing the emergence of the Dirac cone at Γ. (c) Anomalous Hall conductivity of the ReI_3 ML as a function of the Fermi level position, $\Delta\mu = \mu - E_F$, for U_{eff} = 0.8 eV.

Conclusions

In summary, based on first-principles calculations, we have demonstrated that the 2D family of heavier ReX_3 (X = Br and I) are intrinsic half-metals with high Curie temperatures. The results of cohesive energy, phonon spectra and AIMD analysis indicate that they are dynamically and thermodynamically stable. The large SOC drives ReI_3 into a nontrivial topological state with a large Chern number. Moreover, we demonstrate that this QAH nontrivial state persists up to the critical U_{eff}^{crit} value of 0.6 eV, where the atomically thin ReI_3 undergoes a transition from the topological nontrivial to trivial phase with the concomitant onset of a Dirac cone. The nontrivial gapless chiral states and the dependence of the QAH conductivity *versus* the position of the Fermi level provide convincing evidence for the realization of the QAH effect in experiments. Therefore, the family of heavier rhenium trihalides offers great promise for wide application in electronic and spintronic devices.

Conflicts of interest

There are no conflicts to declare.

Acknowledgements

We would like to thank Hugo Aramberri and Farzad Mahfouzi for useful discussions. The work is supported by the NSF-Partnership in Research and Education in Materials (PREM) Grant DMR-1828019 and NSF Grant No. ERC TANMS-1160504.

Notes and references

1 K. S. Novoselov, A. K. Geim, S. V. Morozov, D. Jiang, Y. Zhang, S. V. Dubonos, I. V. Grigorieva and A. A. Firsov, Electric field effect in atomically thin carbon films, *Science*, 2004, **306**, 666.

2 M. Yandong, J. Yu and H. Thomas, Double Dirac point semimetal in 2D Material: Ta_2Se_3, *2D Mater.*, 2017, **4**, 025111.

3 F. Zheng, J. Zhao, Z. Liu, M. Li, M. Zhou, S. Zhang and P. Zhang, Tunable spin states in the two-dimensional magnet CrI_3, *Nanoscale*, 2018, **10**, 14298–14303.

4 S. Zhang, Z. Yan, Y. Li, Z. Chen and H. Zeng, Atomically thin arsenene and antimonene: Semimetal-semiconductor and indirect-direct band-gap transitions, *Angew. Chem.*, 2015, **127**, 3155–3158.

5 N. D. Mermin and H. Wagner, Absence of ferromagnetism or antiferromagnetism in one- or two-dimensional isotropic heisenberg models, *Phys. Rev. Lett.*, 1966, **17**, 1133.

6 C. Gong, L. Li, Z. Li, H. Ji, A. Stern, Y. Xia, T. Cao, W. Bao, C. Wang, Y. Wang, Z. Q. Qiu, R. J. Cava, S. G. Louie, J. Xia and X. Zhang, Discovery of intrinsic ferromagnetism in two-dimensional van der Waals crystals, *Nature*, 2017, **546**, 265.

7 B. Huang, G. Clark, E. Navarro-Moratalla, D. R. Klein, R. Cheng, K. L. Seyler, D. Zhong, E. Schmidgall, M. A. McGuire, D. H. Cobden, W. Yao, D. Xiao, P. Jarillo-Herrero and X. Xu, Layer-dependent ferromagnetism in a van der Waals crystal down to the monolayer limit, *Nature*, 2017, **546**, 270.

8 S. S. Li, Y. P. Wang, S. J. Hu, D. Chen, C. W. Zhang and S. S. Yan, Robust Half-Metallicity in Transition Metal Tribromide Nanowires, *Nanoscale*, 2018, **10**, 15545–15552.

9 L. Zhang, S. F. Zhang, W. X. Ji, C. W. Zhang, P. Li, P. J. Wang, S. S. Li and S. S. Yan, Discovery of a novel spin-polarized nodal ring in a two-dimensional HK lattice, *Nanoscale*, 2018, **10**, 20748–20753.

10 C. Z. Chang, *et al.*, Experimental observation of the quantum anomalous Hall effect in a magnetic topological insulator, *Science*, 2013, **340**, 16770.

11 X. Kong, L. Li, O. Leenaerts, W. Wang, X. J. Liu and F. M. Peeters, Quantum anomalous Hall effect in a stable 1T-YN_2 monolayer with a large nontrivial bandgap and a high Chern number, *Nanoscale*, 2018, **10**, 8153.

12 T. Kurumaji, S. Seki, S. Ishiwata, H. Murakawa, Y. Tokunaga, Y. Kaneko and Y. Tokura, Magnetic-field induced competition of two multiferroic orders in a triangular-lattice helimagnet MnI_2, *Phys. Rev. Lett.*, 2011, **106**, 167206.

13 A. Banerjee, J. Yan, J. Knolle, C. A. Bridges, M. B. Stone, M. D. Lumsden, D. G. Mandrus, D. A. Tennant, R. Moessner and S. E. Nagler, Neutron scattering in the proximate quantum spin liquid α-$RuCl_3$, *Science*, 2017, **356**, 1055.

14 S. Sarikurt, Y. Kadioglu, F. Ersan, E. Vatansever, O. U. Akturk, Y. Yuksel, U. Akinci and E. Akturk, Electronic and magnetic properties of monolayer α-$RuCl_3$: a first-principles, *Phys. Chem. Chem. Phys.*, 2018, **20**, 997.

15 D. Zhong, K. L. Seyler, X. Linpeng, R. Cheng, N. Sivadas, B. Huang, E. Schmidgall, T. Taniguchi, K. Watanabe, M. A. McGuire, W. Yao, D. Xiao, K. C. Fu and X. Xu, Van der Waals engineering of ferromagnetic semiconductor heterostructures for spin and valleytronics, *Sci. Adv.*, 2017, **3**, e1603113.

16 C. Huang, Y. Du, H. Wu, H. Xiang, K. Deng and E. Kan, Prediction of intrinsic ferromagnetic ferroelectricity in a transition-metal halide monolayer, *Phys. Rev. Lett.*, 2018, **120**, 147601.

17 W. B. Zhang, Q. Qu, P. Zhua and C. H. Lam, Robust intrinsic ferromagnetism and half semiconductivity in stable two-dimensional single-layer chromium trihalides, *J. Mater. Chem. C*, 2015, **3**, 12457.

18 N. Miao, B. Xu, L. Zhu, J. Zhou and Z. Sun, 2D intrinsic ferromagnets from van der Waals antiferromagnets, *J. Am. Chem. Soc.*, 2018, **140**, 2417.

19 G. Kresse, Furthmuller, Efficient iterative schemes for ab initio total-energy calculations using a plane-wave basis set, *Phys. Rev. B: Condens. Matter Mater. Phys.*, 1996, **54**, 11169.

20 P. E. Blochl, Projector augmented-wave method, *Phys. Rev. B: Condens. Matter Mater. Phys.*, 1994, **50**, 17953.

21 J. P. Perdew, K. Burke and M. Ernzerhof, Generalized gradient approximation made simple, *Phys. Rev. Lett.*, 1996, **77**, 3865.

22 H. J. Monkhorst and J. D. Pack, Special points for brillouin-zone integrations, *Phys. Rev. B: Solid State*, 1976, **13**, 5188.

23 S. L. Dudarev, G. A. Botton, S. Y. Savrasov, C. J. Humphreys and A. P. Sutton, Electron-energy-loss spectra and the structural stability of nickel oxide: An LSDA+U study, *Phys. Rev. B: Condens. Matter Mater. Phys.*, 1998, **57**, 1505–1509.

24 A. A. Mostofi, J. R. Yates, Y. S. Lee, I. Souza, D. Vanderbilt and N. Marzari, Wannier90: A tool for obtaining maximally-localised Wannier functions, *Comput. Phys. Commun.*, 2008, **178**, 685.

25 Q. S. Wu, S. N. Zhang, H. F. Song, M. Troyer and A. A. Soluyanov, WannierTools: An opensource software package for novel topological materials, *Comput. Phys. Commun.*, 2018, **224**, 405.

26 A. Togo and I. Tanaka, First principles phonon calculations in materials science, *Scr. Mater.*, 2015, **108**, 1.

27 Y. Wang, F. Li, Y. Li and Z. Chen, Semi-metallic Be_5C_2 monolayer global minimum with quasi-planar pentacoordinate carbons and negative Poissons ratio, *Nat. Commun.*, 2016, **7**, 11488.

28 A. Fleurence, R. Friedlein, T. Ozaki, H. Kawai, Y. Wang and Y. Yamada-Takamura, Experimental evidence for epitaxial silicene on diboride thin films, *Phys. Rev. Lett.*, 2012, **108**, 245501.

29 J. Guan, Z. Zhu and D. Tomanek, Phase coexistence and metal-insulator transition in few-layer phosphorene: a computational study, *Phys. Rev. Lett.*, 2014, **113**, 046804.

30 Q. L. Sun and N. Kioussis, Prediction of manganese trihalides as two-dimensional Dirac halfmetals, *Phys. Rev. B: Condens. Matter Mater. Phys.*, 2018, **97**, 094408.

31 M. A. McGuire, G. Clark, S. Kc, W. M. Chance, G. E. Jellison, V. R. Cooper, X. Xu and B. C. Sales, Magnetic behavior and spin-lattice coupling in cleavable Van Der Waals layered $CrCl_3$ crystals, *Phys. Rev. Mater.*, 2017, **1**, 014001.

32 M. Rahman, K. Davey and S.-Z. Qiao, Advent of 2D rhenium disulfide (ReS_2): Fundamentals to applications, *Adv. Funct. Mater.*, 2017, **27**, 1606129.

33 Y.-C. Lin, H.-P. Komsa, C.-H. Yeh, T. Bjurkman, Z.-Y. Liang, C.-H. Ho, Y.-S. Huang, P.-W. Chiu, A. V. Krasheninnikov and K. Suenaga, Single-layer ReS_2: Two-dimensional semiconductor with tunable in-plane anisotropy, *ACS Nano*, 2015, **9**, 11249.

34 S. Tongay, *et al.*, Monolayer behaviour in bulk ReS2 due to electronic and vibrational decoupling, *Nat. Commun.*, 2014, **5**, 3252.

35 R. Gonzalez, R. Chiozzone, C. Kremer, G. De Munno, F. Nicolo, F. Lloret, M. Julve and J. Faus, Magnetic studies on hexaiodorhenate(Iv) salts of univalent cations. Spin canting and magnetic ordering in $K_2[ReI_6]$ with T_c = 24 K, *Inorg. Chem.*, 2003, **42**, 2512–2518.

36 J. B. Goodenough, Theory of the role of covalence in the perovskite-type manganites [La;M(II)]MnO_3, *Phys. Rev.*, 1955, **100**, 564.

37 J. Kanamori, Crystal distortion in magnetic compounds, *J. Appl. Phys.*, 1960, **31**, S14.

38 P. W. Anderson, New approach to the theory of superexchange interactions, *Phys. Rev.*, 1959, **115**, 2.

39 J. Zhou and Q. Sun, Magnetism of phthalocyanine-based organometallic single porous sheet, *J. Am. Chem. Soc.*, 2011, **133**, 15113.

40 Y. P. Wang, S. S. Li, C. W. Zhang, S. F. Zhang, W. X. Ji, P. Li and P. J. Wang, High-temperature Dirac half-metal $PdCl_3$: A promising candidate for realizing quantum anomalous Hall effect, *J. Mater. Chem. C*, 2018, **6**, 10284–10291.

41 M. H. Zhang, C. W. Zhang, P. J. Wang and S. S. Li, Prediction of high-temperature Chern insulator with half-metallic edge states in asymmetry-functionalized Stanene, *Nanoscale*, 2018, **10**, 20226–20233.

42 B. Wang, Q. S. Wu, Y. H. Zhang, Y. L. Guo, X. W. Zhang, Q. H. Zhou, S. Dong and J. L. Wang, High curie-temperature intrinsic ferromagnetism and hole doping-induced half-metallicity in two-dimensional scandium chlorine monolayers, *Nanoscale Horiz.*, 2018, **3**, 551–555.

43 S. Qilong, D. Ying, N. Chengwang, M. Yandong, W. Wei, Y. Lin and H. Baibiao, Lateral topological crystalline insulator heterostructure, *2D Mater.*, 2017, **4**, 025038.

44 D. Xiao, M. C. Chang and Q. Niu, Berry phase effects on electronic properties, *Rev. Mod. Phys.*, 2010, **82**, 1959–2007.

45 J. Heyd, G. E. Scuseria and M. Ernzerhof, Hybrid functionals based on a screened coulomb potential, *J. Chem. Phys.*, 2003, **118**, 8207–8215.

46 W. Li, C. F. Walther, A. Kuc and T. Heine, Density functional theory and beyond for band-gap screening: performance for transition-metal oxides and dichalcogenides, *J. Chem. Theory Comput.*, 2013, **9**, 2950–2958.

47 X.-L. Sheng and B. K. Nikolić, Monolayer of the 5d transition metal trichloride $OsCl_3$: A playground for two-dimensional magnetism, room-temperature quantum anomalous Hall effect, and topological phase transitions, *Phys. Rev. B: Condens. Matter Mater. Phys.*, 2017, **95**, 201402.

48 X. Ni, W. Jiang, H. Huang, K. H. Jin and F. Liu, Intrinsic Quantum Anomalous Hall Effect in a Two-Dimensional Anilato-Based Lattice, *Nanoscale*, 2018, **10**, 11901–11906.